Multi-Frequency Differential Absorption LIDAR (DIAL) System for Aerosol and Cloud Retrievals of CO2/H2O and CH4/H2O

Jasper R Stroud *, Gerd A Wagner , David F Plusquellic *

Posted Date: 3 October 2023

doi: 10.20944/preprints202310.0138.v1

Keywords: DIAL; differential absorption lidar; IPDA; integrated path differential absorption LIDAR; cloud aerosol retrievals

Article

Multi-Frequency Differential Absorption LIDAR (DIAL) System for Aerosol and Cloud Retrievals of CO_2/H_2O and CH_4/H_2O

Jasper R. Stroud [1], Gerd A. Wagner [2] and David F. Plusquellic [1,*]

[1] Applied Physics Division, Physical Measurement Laboratory, National Institute of Standards and Technology, Boulder, CO 80305

[2] German Aerospace Center (DLR), Institute of Technical Physics, Pfaffenwaldring 38-40, 70569 Stuttgart, Germany

* Correspondence: authors: david.plusquellic@nist.gov, jasper.stroud@nist.gov

Abstract: We discuss a remote sensing system that is used to simultaneously detect range-resolved differential absorption LIDAR (light detection and ranging; DIAL) signals and integrated path DIAL signals (IP-DIAL) from aerosol targets for ranges up to 22 km. The DIAL/IP-DIAL frequency converter consists of an OPO pumped at 1064 nm to produce light at 1.6 μm and operates at 100 Hz pulse repetition frequency. The probe light is free space coupled to a movable platform that contains one transmitter and two receiver telescopes. Hybrid photon counting/current systems increase the dynamic range for detection by two orders of magnitude. Range resolved and column integrated dry-air CO_2 and CH_4 mixing ratios are obtained from line shape fits of CO_2 and CH_4 centered at 1602.2 nm and 1645.5 nm, respectively and measured at 10 different frequencies over ≈ 1.5 cm^{-1} bandwidth. The signal-to-noise ratios (SNR) of the IP-DIAL returns from cloud aerosols approach 1000:1 and the uncertainties in the mixing ratios weighted according to the integrated counts over the cloud segments range from 0.1 % to 1 %. The range averaged DIAL mixing ratios are in good agreement with the IP-DIAL mixing ratios at the 1 % to 2 % level for both CO_2 and CH_4. These results can serve as a validation method for future active and passive satellite observational systems.

Keywords: DIAL; differential absorption lidar; IPDA; integrated path differential absorption LIDAR; cloud aerosol retrievals

1. Introduction

Active remote sensing using differential absorption LIDAR (DIAL) [1–4] and integrated path differential absorption LIDAR (IP-DIAL) [5–9] provides the necessary measurement precision and accuracy to study greenhouse gas (GHG) concentrations in the atmosphere. Of particular importance, the dry-air mixing ratios of the GHGs, CO_2 and CH_4, can be monitored on a global scale using satellites for climate studies [10–13] and with ground-based systems for local and large city emission studies [14]. Airborne systems have been used to develop spaceborne platforms and to later calibrate ground-based and spaceborne sensors [7,15–17]. Largely overcoming the inherent limitations of passive systems [18,19], DIAL and IP-DIAL systems can provide the measurement data to study and assess the current state and dynamics of Earth's ecosystem under GHG fluctuations.

Current DIAL and IP-DIAL system development for remote sensing of CO_2 and CH_4 focuses on the NIR (near infrared) spectral regions (1572 nm (CO_2), 1602 nm (CO_2), 1645 nm (CH_4), 2050 nm (CO_2)). The main technological challenges are the selection of a suitable laser source and detector, both of which have been the subject of numerous studies for current research systems over the past decade (see the overview given in [9]). The latest developments for DIAL [4] and IP-DIAL [7,9] systems make use of multiple frequencies to sample the absorption line profile and use subsequent spectral line shape fitting to obtain the GHG mixing ratios. This method is found here to be particularly suitable for complicated line shapes consisting of multiple underlying transitions (e.g.,

Preprints (www.preprints.org) | NOT PEER-REVIEWED | Posted: 3 October 2023 doi:10.20944/preprints202310.0138.v1

CH_4) and/or multi-species determinations (e.g., CH_4 or CO_2 and H_2O). Additional advantages have been realized in studies to and through clouds to enhance sensitivity. For example, previous IP-DIAL studies from aircraft measured 30 points across the CO_2 line shape to perform studies to cloud tops and through clouds to the surface [7]. Cloud targets have also found importance in the specification of the overall spectral purity of the DIAL frequency converter from comparisons of the online and offline frequency returns [20].

The work presented here demonstrates the application of a 10-frequency DIAL system to study GHG mixing ratios of CO_2 and H_2O (denoted CO_2/H_2O) and CH_4/H_2O from aerosol and cloud aerosol returns using an optical parametric oscillator (OPO) [21]. We present the data processing and mixing ratios obtained from IP-DIAL retrievals to clouds and make comparisons to the column averaged DIAL mixing ratios to validate the methods and potentially identify disagreements with currently available line shape models.

This paper is structured as follows: Section II.1 presents the experimental 10-frequency OPO transmitter and movable transceiver platform used to perform DIAL and IP-DIAL studies of CO_2/H_2O and CH_4/H_2O. Section II.2 discusses the DIAL and IP-DIAL data processing including the line shape fitting procedure to obtain GHG concentrations and mixing ratios. Section II.3 reviews the latest spectroscopic improvements to the CH_4 line shape near 1645 nm. Section III presents the data processing for IP-DIAL retrievals from diffuse clouds (III.1), the IP-DIAL results for CO_2/H_2O and CH_4/H_2O (III.2), the DIAL results for CO_2/H_2O and CH_4/H_2O (III.2), and an overall comparison of the mixing ratios obtained from IP-DIAL, DIAL and a (cavity ringdown) point sensor. A discussion of the uncertainties relative to satellite calibration requirements is given in Section IV. The paper closes with conclusions and outlook in Section V.

2. Experiment

2.1. Combined DIAL and IP-DIAL system

A schematic of the overall system setup at NIST is shown in Figure 1 and is similar to the system described in [2]. The system specifications are given in Table 1 [22]. Briefly, the seed source of the frequency converter is based on the fixed frequency output of an external-cavity diode laser (ECDL). A portion (10 %) of the fiber-coupled ECDL output is first frequency shifted in an acousto-optic modulator (AOM), modulated in an electro-optic phase modulator (EOM_1) and then free-space coupled and mode-matched into a 50 cm Invar confocal filter cavity that is used to frequency lock the laser to the cavity in reflection (Pound-Drever-Hall method [23]). The remaining 90% is fiber coupled to a second broadband EOM_2 that is driven by a fast-switching microwave synthesizer. The microwave (MW) frequencies are defined such that only one of the second-order harmonics from the EOM (i.e., shifted from the carrier by 2×MW frequency) is transmitted through the filter cavity [9] at any given time with high spectral purity (> 30 dB).

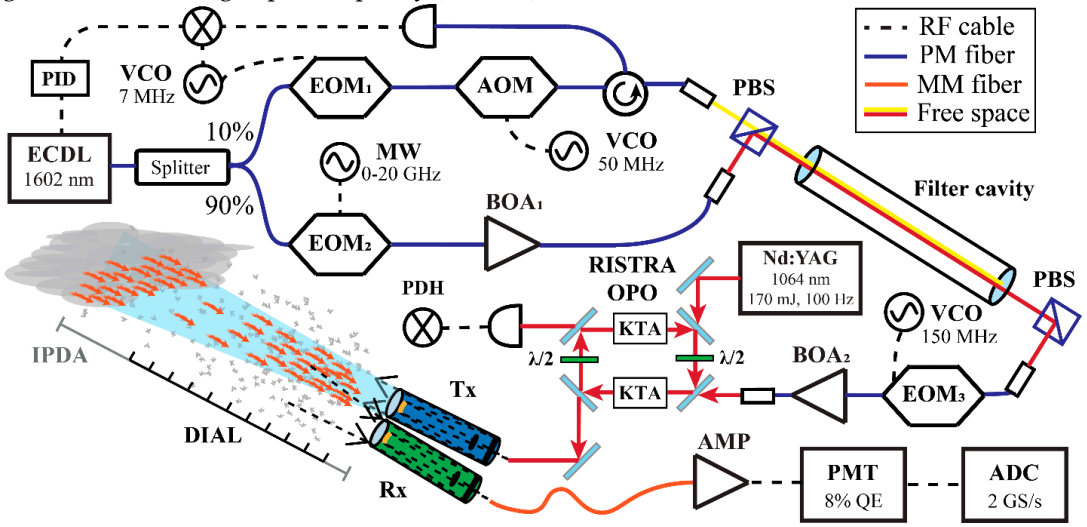

Preprints (www.preprints.org) | NOT PEER-REVIEWED | Posted: 3 October 2023 doi:10.20944/preprints202310.0138.v1

Figure 1. DIAL/IP-DIAL system overview. The ECDL output is split into two legs for frequency offset locking the laser to the filter cavity (10 % leg) and for fast 2nd-order EOM sideband tuning through the filter cavity (90 % leg).The filter cavity output seeds an image rotating OPO to generate ≈ 5 mJ pulses at 100 Hz PRF. The free spaced beam is actively locked to a movable platform (0°-30° in inclination and ±30° laterally) and transmitted from a beam expanding telescope (Tx). The receiver setup (Rx) consists of near-field and far-field (FF) telescopes (although only the FF data is discussed for these studies). Both receivers are fiber coupled to photomultiplier tubes (PMT) housed in a temperature-cooled box. Optical bandpass filters (not shown) for CO_2/H_2O and CH_4/H_2O are centered at 1602.2 nm and 1645.5 nm have peak transmission of >90 % and a full width at half maximum (FWHM) of 2 nm. The NF and FF channels are amplified with a transimpedance gain of 5 kV/A (AMP) and digitized (ADC) at 2×10^9 samples per second with 8-bit resolution. The photon counts and current for each receiver are co-added separately for each transmitted frequency resulting in 40 data segments that are stored every 10 seconds in Network Common Data Form file format (NetCDF). (ECDL: external cavity diode laser, PID: proportional-integral-differential controller, VCO: voltage-controlled oscillator, RISTRA OPO: KTA: potassium titanyl arsenate, MW: microwave synthesizer, BOA: booster optical amplifier, EOM: electro-optic modulator, AOM: acousto-optic modulator, ADC: analog-to-digital converter, PBS: polarizing beam splitter, AMP: electronic amplifier.

The 10 transmitted sideband frequencies that define a scan are sequentially generated at a 100 Hz pulse repetition frequency (PRF). The frequency sequence is continuously repeated every 100 ms to give a 10 Hz overall scan rate. In second order, the spectral bandwidth coverage over the (±) sidebands is ≈ 50 GHz and centered near the ECDL frequency. The fiber-coupled output of the filter cavity is passed through EOM_3 driven at 150 MHz and amplified to ≈ 10 mW to enable the PDH lock of the optical parametric oscillator (OPO) to each injection seeded frequency.

Table 1. Specifications of the OPO based DIAL/IP-DIAL system[a] [22].

Frequency Converter:		
Wavelength coverage	1600 nm to 1647 nm	New Focus, ECDL
Number of frequencies	10	Spectral coverage ≈ 80 GHz
PRF, SRF	100 Hz, 10 Hz	1064 nm, Coherent Infinity
Pulse energy	7 mJ	at E_P=175 mJ
Microwave Synthesizer	20 GHz bandwidth	MW, Anritsu, MG37022A
Electro-optic modulator	10 GHz bandwidth	EOM_1, Thorlabs
Acousto-optic modulator	50 MHz	Brimrose
Electro-optic modulator	20 GHz bandwidth	EOM_2, EOSpace
Invar filter cavity	300 MHz free spectral range	Burleigh, CFP-500, l = 0.5 m
Spectral purity	>99.9%	Filter cavity finesse ≈ 500
Booster optical amplifier	20 mW, <20 dB gain	BOA, Thorlabs, S9FC1082P
Pulse length (FWHM)	< 3 ns	Pump pulse ≈ 3 ns FWHM
Spectral linewidth (FWHM)	190 MHz	Near transform limited
Two OPO KTA Crystals	10x10x15 mm^3, θ=67.4°, φ=0°	Optical Platz, Inc
OPO	RISTRA, twisted rectangle	AS Photonics, Inc
Tx/Rx optics and detectors:		
Tx beam diameter	127 mm	Ritchey-Chrétien, Orion
NF Rx telescope diameter	279.4 mm	Schmidt-Cassegrain, Celestron
FF Rx telescope diameter	406.5 mm	Schmidt-Cassegrain, Meade
Bandpass filter, 1645.5 nm	1.9 nm (FWHM), T>90%	> 5 OD rejection, Alluxa
Bandpass filter, 1602.2 nm	2.0 nm (FWHM), T>90%	> 5 OD rejection, Materion
Neutral density filter	0.1, 0.3, 0.6, and 1 OD	Thorlabs
Fiber coupled	300 μm aperture	1 m cable length
PMT detection	~2% QE	Hamamatsu H12397-75

PMT detection	~8% QE	Hamamatsu H12397-75 SEL
Data acquisition:		
Transimpedance amp	5 kV/A, $\tau_{3dB} \approx 1$ ns	Femto HCA-400M-5K-C
Digitizer	8 bits, 2 GS/s, 2 channels	GaGe CobraMax CSE24G8
Raw data storage	10 s accumulation	NetCDF4 file format
Range bin resolution	250 m to 500 m	Defined in post-processing
Temporal resolution	5 min	DIAL concentration average

[a]NF: near-field, FF: far-field, PRF: pulse repetition frequency, SRF: scan repetition frequency, Ep: pump pulse energy, FWHM: full width at half maximum, FOV: field of view, PMT: photomultiplier tube, QE: quantum efficiency, T: transmittance, Tx: transmitter, Rx: receiver.

The OPO contains two KTA crystals (type I phase matching) in a twisted ring resonator configuration for image rotation [24–26] and is pumped at 100 Hz PRF with 170 mJ/pulse at 1064 nm using an injection-seeded Nd:YAG laser. The signal wave output pulse energy used is ≈ 5 mJ and has a measured near-transform-limited 190 MHz line width [4]. The KTA crystals are cut so that the signal wave can be angle tuned over the spectral region from 1600 nm to 1650 nm to access the strongest lines in the 30013-00001 band of CO_2 (the R(22e) line at 1602.2 nm) and in the 2 ν_3 band of CH_4 (the R(6) manifold at 1645.2 nm). In both cases, nearby water lines are also sampled to determine dry-air mixing ratios. The signal wave of the OPO output is separated from the remaining pump and OPO frequencies using a home-built prism beam separator containing four SF_6 60° prisms in a folded wavelength-compensating-path configuration and then propagated along a coudé path to a movable platform (91 cm x 152 cm). Two galvanometers in the path are used for steering the beam to an expanding telescope for Class I level transmission using both feed-forward and feed-back signals derived from the position of the pneumatic cylinder and a quadrant photodetector, respectively.

Two receiver telescopes are also mounted on the movable platform and consist of a near-field (NF) and far-field (FF) telescopes (data from the FF system was primarily used in this study). Both are equipped with altitude/azimuth mount for alignment with the fixed transmitted beam. The collected light is coupled into 1 mm multi-mode fibers and then free-space coupled to near-IR photomultiplier tubes (PMT). Narrow bandpass filters are used for CO_2 at 1602.2 nm and CH_4 at 1645.5 nm. To aid in reducing background light during daytime viewing, filter wheels are available with optical densities from 0 to 3. The movable platform weighing more than 300 kg can be scanned laterally by ± 30° using a stepper motor control stage and in altitude from 0° to 30° using a pneumatic control cylinder.

Two spectral regions targeted for these studies are illustrated in Figure 2a,b. For the CO_2/H_2O region shown in Figure 2a, five frequencies are selected on the R(22e) CO_2 line of the 30013-0001 band at 1602.205 nm (6241.40 cm^{-1}) and two frequencies on the H_2O line pair at 1602.133 nm and 1602.102 nm (6241.68 cm^{-1} and 6241.81 cm^{-1}), and the remaining 3 frequencies sample the baseline regions at both ends of the spectrum. For CH_4/H_2O region shown in Figure 2b, six frequencies sample across the doublet structure of the R(6) manifold of the 2ν_3 band centered at 1645.534 nm (6077.05 cm^{-1}), one frequency on the H_2O line at 1645.471 (6077.28 cm^{-1}) and the remaining three frequencies sample the baseline regions on both ends. Over a range of 250 m (500 m path length), the optical densities of CO_2 and CH_4 are near 4% for ambient levels of CO_2 (≈ 420 ppm) and CH_4 (≈ 2 ppm).

Preprints (www.preprints.org) | NOT PEER-REVIEWED | Posted: 3 October 2023 doi:10.20944/preprints202310.0138.v1

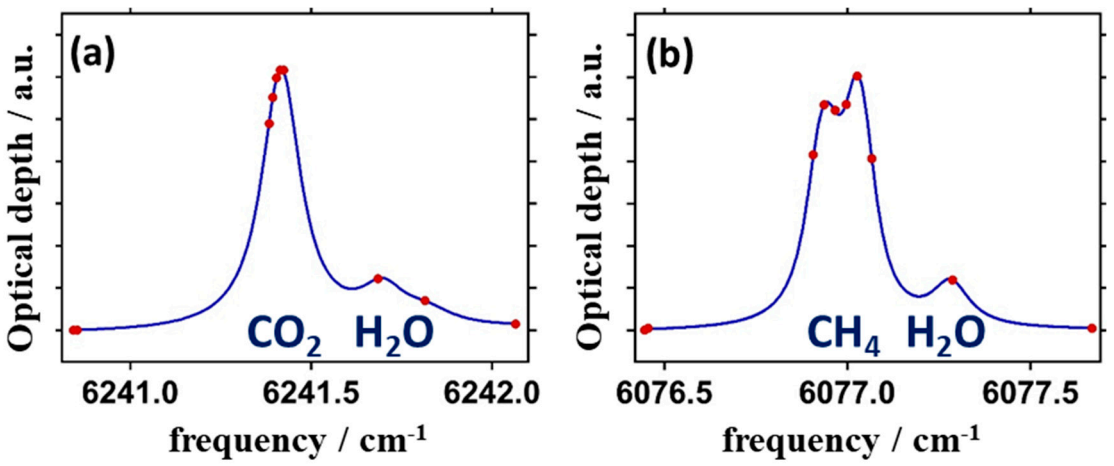

Figure 2. The spectral regions selected to measure the mixing ratios of (a) CO_2 and H_2O and (b) CH_4 and H_2O. The ten frequencies used to probe the lines are shown with solid (red) dots where the first two frequencies are nearly on top of one another.

2.2. *Raw data processing and concentration fitting procedure*

The pre-processing of the raw data follows the procedure discussed previously [1]. Briefly, a dual channel 8-bit digitizer samples the output voltages of the PMTs at a rate of 2 GS/sec. This is fast enough to resolve the amplified photon current signal from the PMT with 7 samples across the full width of each count. Double counting is prevented by skipping 6 samples following threshold detection. In software, the accumulated counts and current for both the NF and FF receivers are saved separately on 10 s intervals for each frequency in NetCDF format.

The processing begins with the accumulation of the photon counts and current over 10 consecutive points which reduces the range resolution to ≈ 1.5 m. For all ten frequencies, a non-linear least square fit (NLLSF) is used to determine the saturation parameter to correct for pulse pileup error. The individual parameters for each frequency and interval are typically fit over a region where the count rates range between N = (1-5) x10^6 counts/s. The frequency averaged saturation parameter over all intervals is then fixed and NLLSF repeated to fit the current to the photon count signal using a scalar and offset parameter on each interval [27]. This hybrid detection scheme extends the linearity of the photon counting system to several billion counts/s. These same parameters are used for splices over the enhanced backscatter regions from cloud returns when the saturated count threshold levels are exceeded.

To fit the concentrations of the DIAL and IP-DIAL profiles at each altitude (i.e., at each temperature and pressure), we first generate line shape templates for CO_2 and CH_4 at 400 ppm and 2 ppm, respectively. Given that the CO_2 line is a single transition and that we use only 5 online frequencies near the peak of the absorption to measure the line, a higher accuracy line shape function that includes line mixing and speed dependent effects was not necessary. Therefore, the template line shape function used was a Voigt profile based on the line broadening and shift parameters reported in the HITRAN 2020 database [28]. However, for CH_4, the most accurate line shape function was required and discussed separately below. Voigt functions for the nearby water vapor lines were added to the overall profile at the 1 % (10,000 ppm) level.

For the range resolved DIAL concentrations, the raw data are processed at the 10 frequencies using a numerical procedure described in [4]. The differential absorption optical depth, $DAOD(R,\nu_i)$, at each of the 10 frequencies, ν_i, is first determined from the integrated photon count data, N_i, at range, $R=(R_1 + R_2)/2$ with range resolution, $\Delta R=(R_2-R_1)$, from

$$DAOD(R,\nu_i) = ln\left(\frac{N_i(R_1)N_b(R_2)}{N_b(R_1)N_i(R_2)}\right) \quad (1)$$

where N_b is the one of the background frequencies conveniently chosen as the first point (i.e., $DAOD(R,\nu_1) = 0$) and R=0 is where the pulse leaves the transmitter telescope. From our prior DIAL

Preprints (www.preprints.org) | NOT PEER-REVIEWED | Posted: 3 October 2023 doi:10.20944/preprints202310.0138.v1

study of CO_2 [4], the OPO signal-wave frequency is known to be shifted by ≈ 120 MHz relative to the input seed frequency. To account for this shift (as well as other frequency drift factors), the initial center frequencies were determined from the fitted profiles obtained from averaging over of the first 6 range bins. Model-based adjustments to the center frequencies and line shapes were then made for changes in altitude. The final fits of optical density at the 10 frequencies were performed following iterative updates of the scaled templates. All components of a given species were scaled together to give concentrations in μmole/mole (ppm) for CO_2 and CH_4 and in percent mol/mol (PCM) for water vapor. We also note that the line width of the laser (190 MHz) was added in quadrature to the Gaussian component of the profile and the temperatures and pressures used at each altitude were derived from the U.S. Standard Atmosphere model [29] after correction for the weather station data at the base altitude of the transmitter in Boulder (1655 m). For the IP-DIAL measurements over regions with increasing altitude, the path length is first divided into equal sections with temperature and pressure corrected for altitude and the line shapes over each section are averaged prior to performing fits. Further details of the IP-DIAL processing procedures are given below.

2.3. Methane line shape profile

The line shape function of the R(6) manifold of the $2\nu_3$ band of CH_4 is complicated given that it is an unresolved profile under atmospheric conditions consisting of 6 major lines. This complexity has likely contributed to the significant changes in the cross sections and Voigt line shape parameters reported in the HITRAN databases over the past 20 years. Moreover, the line shape is further complicated by line mixing and speed-dependent effects which cannot be modeled by a simple Voigt profile used in HITRAN. Given the importance of the R(6) line for the upcoming active satellite IPDA measurements from MERLIN [10,11], several cavity ringdown studies have been performed to (i) measure the precise line centers of the 6 lines using saturation spectroscopy [30,31] and (ii) fit the temperature and pressure dependence of these transitions [32,33] to the Hartmann-Tran profile (HTP) [34]. As a result of the high sensitivity of the IP-DIAL returns, we found it necessary to make use of this model to minimize the residuals. It is further noted that the overall integrated intensity of the HTP R(6) profile is scaled to that of HITRAN 2020 [33] and that additional studies are underway at NIST to link the intensity scale to the International System of Units (SI).

3. Results

3.1. IP-DIAL studies of the LIDAR returns from diffuse clouds

The measurements of the CO_2/H_2O region were performed over the 7 h nighttime period on Nov. 24, 2021 beginning at 8:08 PM local time. The telescope was at an inclination of 2.5° off the horizon and pointed ≈ -10° off North across the city of Boulder. The measurements of the CH_4/H_2O region were performed over the 5 h nighttime period on Apr. 28, 2022 beginning at 10:05 PM local time. The telescope was at an inclination of 10.5° and pointed 2.4° off North across the city of Boulder.

The range corrected LIDAR returns from the first offline frequency in the CO_2 region are shown in Figure 3b for one of the initial 10 min intervals. A cross section cut of the LIDAR returns is shown in Figure 3a at each of the 10 different frequencies. In the first 2 h period, normal aerosol returns extend to about 10 km, at which point the scattering is significantly enhanced upon passing through a ≈ 2 km cloud segment centered at ranges from 11 km to 15 km. The offline cloud signal returns (shown in blue) exceed 200×10^6 count/s and are of the same magnitude as seen near full overlap at 0.5 km. From a comparison of the online (red) and offline returns in the cloud region, the CO_2 absorption signal over this 20+ km pathlength represents > 70% fractional absorption.

Preprints (www.preprints.org) | NOT PEER-REVIEWED | Posted: 3 October 2023 doi:10.20944/preprints202310.0138.v1

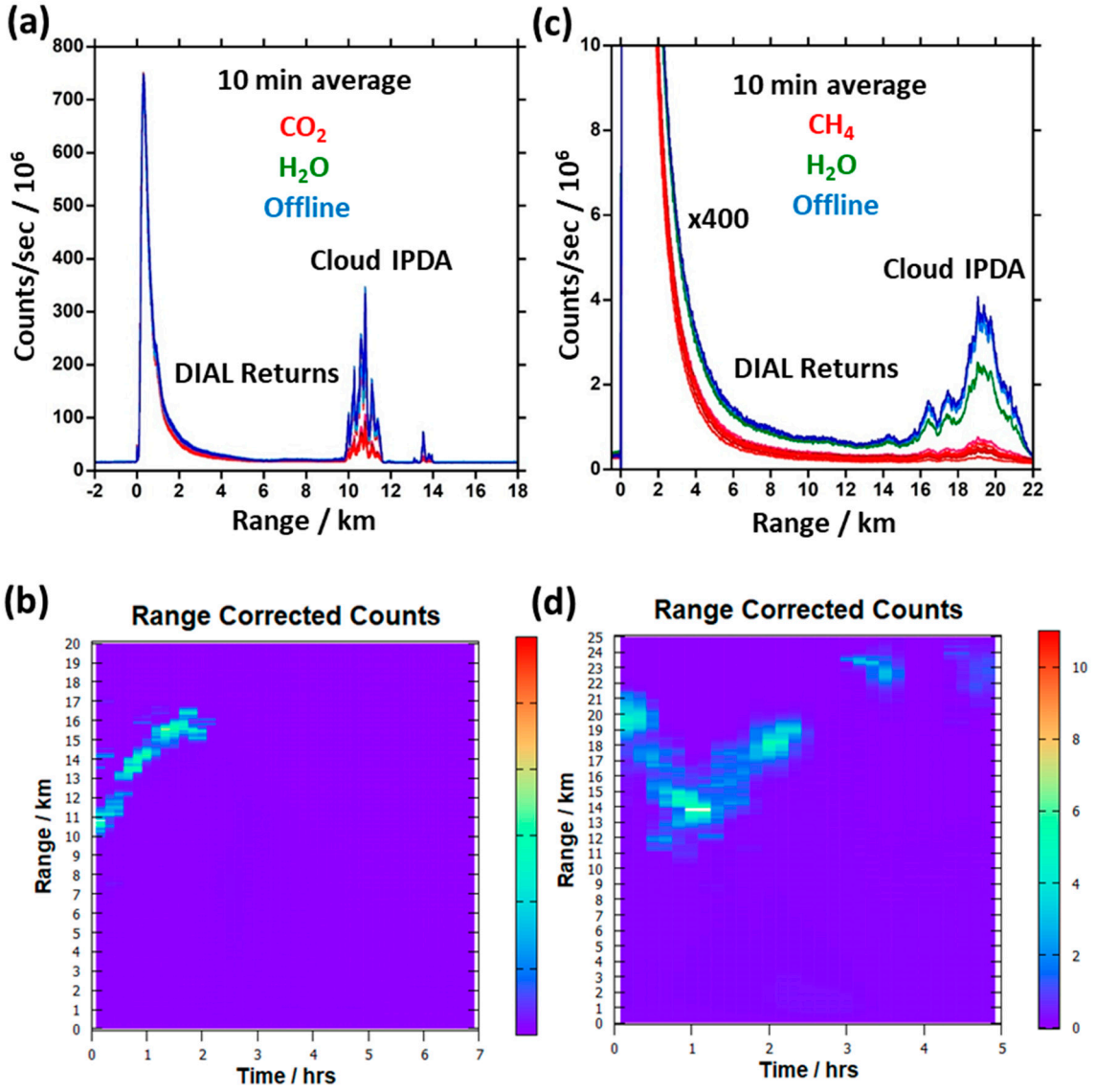

Figure 3. (a) The unscaled range-resolved signal returns from natural aerosols for the CO_2 region out to 10 km and from cloud aerosols from 10 km to 12 km. The inclination of the receiver was 2.5° off the horizon. The data were obtained on Nov. 24, 2021. The 5 darker colors are from the offline regions (blue) and the 5 lighter colors are from the online CO_2 (red) and H_2O (green) returns. (b) The range and background corrected LIDAR map for the first offline frequency is shown for the full measurement period. (c) Unscaled range-resolved signal returns from natural aerosols are shown for the CH_4 region out to 15 km and from cloud aerosols from 14 km to 22 km. The inclination of the receiver was 10.5° off the horizon. The data were obtained on Apr. 28, 2022. The 3 darker colors are from the offline regions (blue), and the 6 lighter colors are from the online CH_4 (red) and H_2O (green) returns. (d) The range and background corrected LIDAR map for the first offline frequency is shown for the full measurement period.

The range corrected LIDAR returns for the CH_4 region are shown in Figure 3d and a cross section cut of the raw returns at all 10 frequencies is shown in Figure 3c for ranges up to 22 km. The enhanced backscatter from the more diffuse clouds extends over a 6 km range beginning at ≈ 14 km and is 50 times less than the CO_2 region shown in Figure 3a. With the pathlength being nearly double that of the CO_2 region, online fractional absorption of the CH_4 region is > 90 % of the offline returns. Furthermore, the larger returns for the CO_2 region are above the saturated count threshold and require the use of the PMT's current channel, while the returns in the CH_4 region remained linear in

Preprints (www.preprints.org) | NOT PEER-REVIEWED | Posted: 3 October 2023 doi:10.20944/preprints202310.0138.v1

photon counts. Therefore, these two systems represent near limiting cases for backscatter studies from clouds.

The range dependence of the optical depth gives a better representation of the linearity and signal-to-noise ratio of the returns. The natural logarithm of the ratios for each frequency, *k*, relative to the first offline color gives the optical depth, *OD(R)*, as a function of range, *R*, from,

$$OD_k(R) = \ln\left(\frac{N_k(R)}{N_1(R)}\right) \quad (2)$$

where $N_k(R)$ are the accumulated counts in a 10 min interval. Since the online optical depths are proportional to the GHG concentrations at the different frequencies, they are expected to increase approximately linearly with range, as is evident in Figure 4a,b, respectively. The SNR decreases with range since the accumulated counts decrease by the inverse square of the range (i.e., SNR(R) ≈ $\sqrt{N_k/R^2}$ in a uniform aerosol field). However, beyond 10 km in Figure 4a, the SNR increase significantly from the enhanced backscatter from the cloud aerosol returns. Furthermore, the near linear increase in $OD_k(R)$ across the cloud region indicates sufficient transparency to perform integrated path measurements. A similar trend is observed in Figure 4b for CH_4/H_2O, although the enhancement in SNR from cloud aerosols is not as pronounced because the 2-fold increase in range results in a significant decrease in the total backscatter.

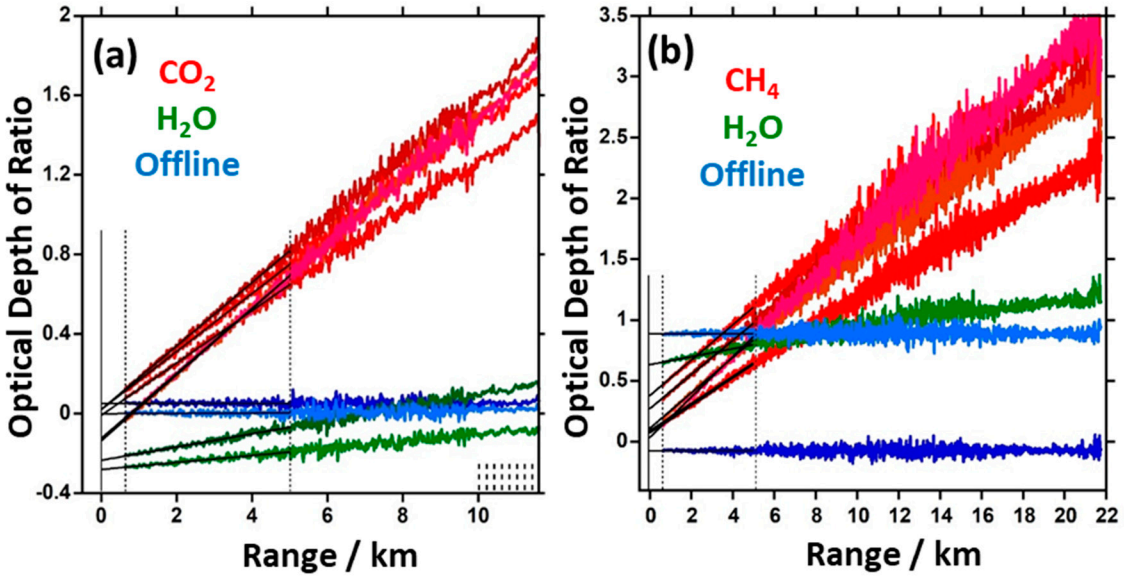

Figure 4. (a) The log ratios, $\ln\left(\frac{N_k(R)}{N_1(R)}\right)$, (optical depth) for CO_2/H_2O as a function of range, illustrating their near linear increases up to and through the cloud (online CO_2 or CH_4: red, online H_2O: green, offline: blue). The enhanced SNRs after 10 km are from the more than 100-fold increase in back scattered counts from the cloud aerosol signal returns. b) The near linear optical depth increases for CH_4/H_2O are shown as a function of range. The enhanced SNRs from 14 km to 22 km are from the >10-fold increase in back scattered counts from the cloud aerosol signal returns. The solid black lines overlaying the data are from linear fits of the data between the vertical dashed lines (0.625 km to 5 km) after correction for small variations in concentration and line shape. The line intercepts for each color at the solid vertical line (i.e., R=0) are proportional to the initial laser pulse energies of the laser. The vertical dashed lines in the lower right corners serve to illustrate how the processed data are binned over the enhanced backscatter regions.

In contrast to DIAL processing that is laser energy independent (see Eqs. 1 and 2), the IP-DIAL processing of the integrated cloud returns requires knowledge of the relative energy in each pulse. The integrated path optical depth, $IPOD_k(R)$, of point, *k*, can be expressed as,

$$IPOD_k(R) = \ln\left(\frac{N_1(0)}{N_k(0)}\right) + \ln\left(\frac{N_k(R)}{N_1(R)}\right) \quad (3)$$

Preprints (www.preprints.org) | NOT PEER-REVIEWED | Posted: 3 October 2023 doi:10.20944/preprints202310.0138.v1

where the first term on the right represents the log ratio of the transmitted laser pulse energies (LPE). Typically, for IP-DIAL studies, the pulse energies of the reference channel are measured independently by sampling the output beam before expansion and transmission [35],9]. However, unlike the output from single-mode fiber-based sources [9], the shape of our free-space OPO beam depends slightly on frequency. Consequently, the energy ratios of the signal and reference channels at the different frequencies were found to vary slowly with time. Other factors such as the unmatched filter bandwidths and differing detector quantum efficiencies also contributed to the observed variations in these ratios. As previously discussed [35], careful designs and detailed calibrations are required to proportionally match the relative energies in the signal and reference channels.

The simultaneous measurement of DIAL and IP-DIAL returns enables an alternative method to determine the LPEs. The method takes advantage of the linear range dependence of the optical depths shown in Figure 4a,b. From Eq. 3, the LPEs can be obtained from the linear fits of this data following small corrections for changes in concentration and altitude. By extrapolating the curves back to when the laser (OPO) pulse leaves the transmitter (R=0), the LPE terms in Eq. 3 are obtained directly. The curve fits are performed over the region from 0.625 km to 5 km (see vertical dashed lines in Figure 4a,b) where the intercepts at R=0 represent the LPEs for each 10 min average. The uncertainties of the intercepts are typically < 0.005 in optical density and therefore have a minor impact on the fitted concentrations.

3.2. IP-DIAL studies of CO_2/H_2O and CH_4/H_2O

Unlike hard target backscatter where the integrations are effectively performed over the width of the laser pulse, the diffuse nature of cloud aerosols leads to an extended source of the enhanced backscatter that ranges from 2 km for the CO_2/H_2O region to > 6 km ranges for the CH_4/H_2O region. The inclination angle for the CO_2/H_2O study was 2.5° which corresponds to clouds at an altitude of ≈ 0.44 km at a range of 10 km from the transmitter. The inclination angle for the CH_4/H_2O study was 10.5°, which corresponds to clouds at an altitude of ≈ 3.5 km at distance of 19 km from the transmitter. Since the model line shape function depends on temperature and pressure, it will change with altitude over the extended region of the cloud. As a result, separate calculations are required over multiple and contiguous range bin slices to properly model the integrated path concentrations.

The path integrated concentrations to cloud targets were determined on 10 min intervals, and fits were performed over consecutive 250 m slices where for each slice, the beam path was divided into typically 5 or more sections depending on the inclination of the transceiver system. As described above, the line shape for each section was calculated at the temperature and pressure predicted using the U.S. Standard Atmosphere model [29] and the concentrations for each slice were determined from fits to the averaged line shape over these sections. The parameters varied in the NLLSF included a baseline offset, slope and the concentrations of CO_2 or CH_4 and H_2O where all lines of the given species were scaled together as a group.

The series of best-fit line shapes to the absorption data over the CO_2/H_2O and CH_4/H_2O regions are shown on 250 m intervals in Figure 5a,b, respectively. The absorption data were obtained for a single 10 min interval near the beginning of both measurement periods (see Figure 4a,b) after processing using Eq. (3). The fit residuals shown in the sub-panels increase with range as expected for ≈ 1/*R* decrease in SNR. However, in the cloud aerosol region of CO_2/H_2O between 12 km and 13.5 km, the SNR improves significantly, leading to an obvious reduction in the scatter of the residuals. The improvement in the corresponding cloud aerosol region of CH_4/H_2O between 18 km and 22 km is not as apparent because of the much weaker signal returns.

Preprints (www.preprints.org) | NOT PEER-REVIEWED | Posted: 3 October 2023 doi:10.20944/preprints202310.0138.v1

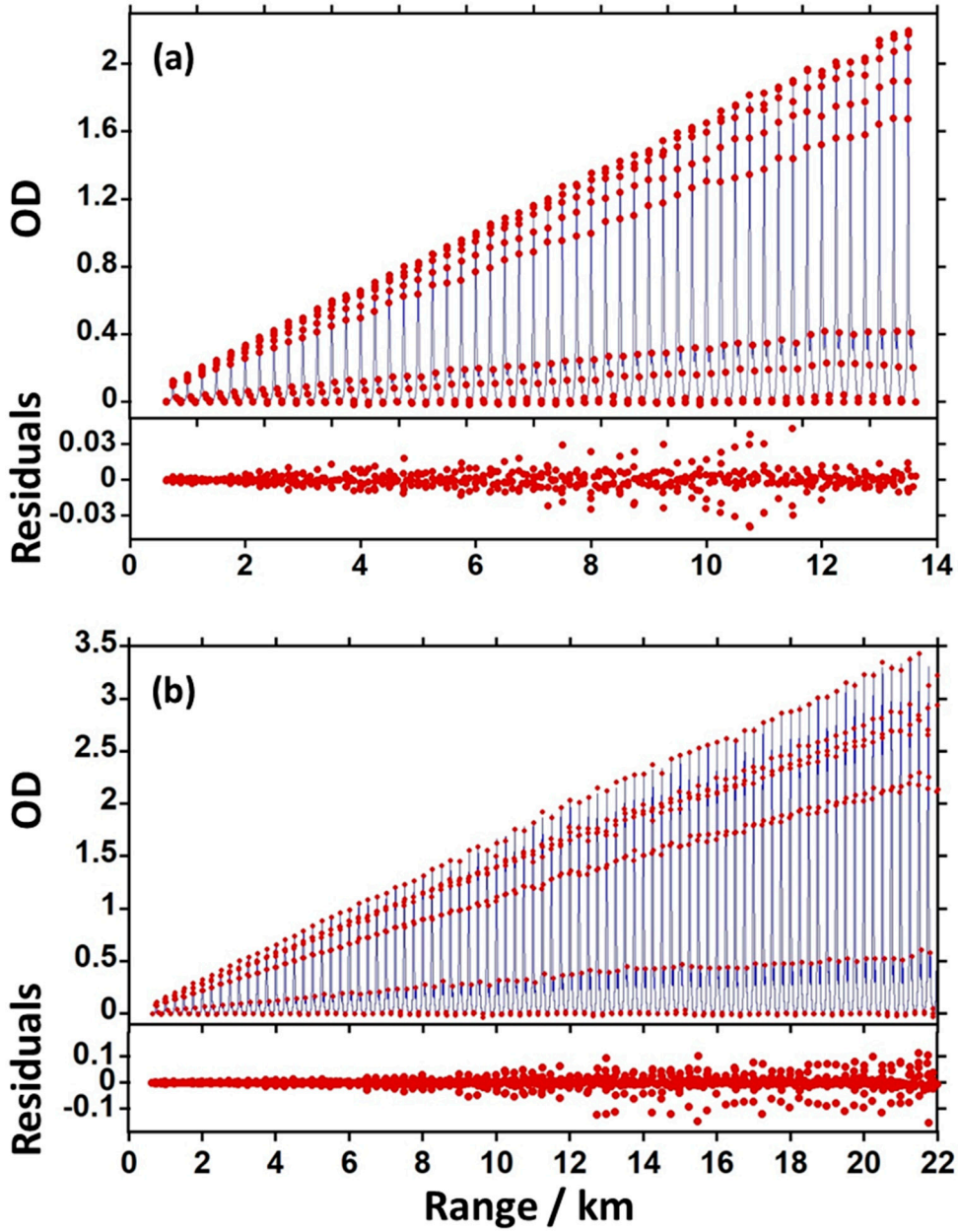

Figure 5. Integrated path (IP-DIAL) line shape fits as a function of range over a single 10 min interval of the (a) CO_2/H_2O region and (b) CH_4/H_2O region. Residuals from the fits are shown in the lower panels. The reduction in the residuals in (a) from 12 km to 13.5 km results from large enhancement in backscatter from cloud aerosols. For the CH_4/H_2O fits in (b), the reduction in the residuals is not as obvious c returns.

More detailed views of the fits and residuals are illustrated in Figure 6a–d at both short range from normal aerosol returns (1.5 km to 1.75 km) and at long range from cloud aerosol returns (near 12.5 km for CO_2 and 18.75 km for CH_4). In both short and long range, the relative magnitude of the residual scatter for CO_2/H_2O is on the order of 1 % relative to the peak online optical density. For the CH_4/H_2O region, residuals are again near 1 % at short ranges but increase to ≈ 3 % at long ranges. This increase may arise from the very low online count rates at 19 km (see Figure 3c). However, some systematic structure appears to remain in the residuals which may suggest an error in the calculated temperature and pressure (T&P) profile. The additional uncertainties (biases) of the T&P profile and those associated with the spectroscopic parameters are discussed in Section IV. We note that relative

Preprints (www.preprints.org) | NOT PEER-REVIEWED | Posted: 3 October 2023 doi:10.20944/preprints202310.0138.v1

to CO_2, the CH_4 cloud region was measured at more than eight times the altitude (0.43 km vs 3.5 km), resulting in significant gradients in the temperature and pressure over the range. The model line shape narrows at this altitude and contributions to the average line shape lead to a more well-resolved doublet profile as the data in Figure 4d reveal.

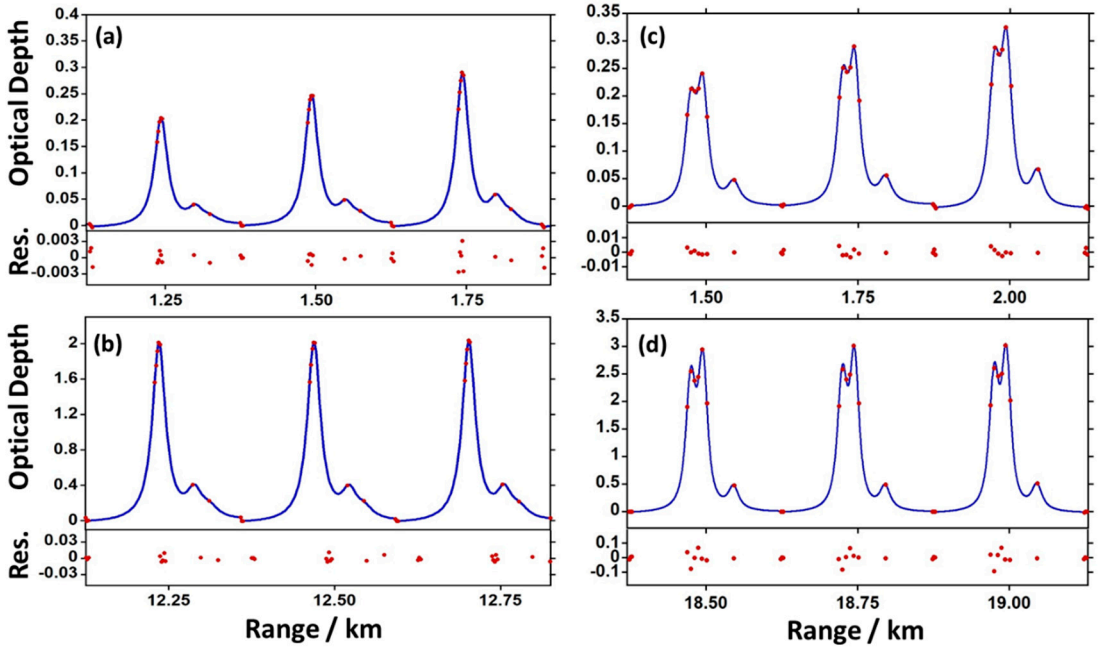

Figure 6. The IP-DIAL data (red dots) and best-fit profiles in the CO_2/H_2O region shown at different ranges centered at (a) 1.5 km and (b) 12.5 km and in the CH_4/H_2O region shown at ranges centered at (c) 1.75 km and (d) 18.75 km. The frequency axes of each profile (not shown) span about 1.5 cm^{-1}. The residuals are shown below each profile relative to calculated line shapes (blue) from HITRAN 2020 for the CO_2/H_2O regions and from HTP for CH_4/H_2O regions.

The enhanced backscatter from the extended cloud aerosol regions affords an opportunity to reduce the measurement uncertainties of the column-averaged mixing ratios. The column integrated concentrations may be obtained from the mean over all slices, $\bar{x}_{wtd}$, each weighted by the integrated counts for that slice relative to the total returns (i.e., total weight). The uncertainties, s_{wtd}, can then be evaluated from the weighted standard deviation of the mean of the slices as given by

$$\bar{x}_{wtd} = \frac{\sum_{i=1}^{n} w_i x_i}{\sum_{i=1}^{n} w_i} \quad (4)$$

$$var(x)_{wtd} = \left[\frac{\sum_{i=1}^{n} w_i x_i^2}{\sum_{i=1}^{n} w_i} - (\bar{x}_{wtd})^2\right] \frac{n}{n-1} \quad (5)$$

$$s_{wtd} = \sqrt{\frac{var(x)_{wtd}}{n}} \quad (6)$$

where w_i are the weights of the individual measurements, x_i, n is the number of slices and $var(x)_{wtd}$ is the weighted variance.

The averaging procedure has been applied over a large enough range to capture all of the cloud features in both regions. Signals below a certain threshold in the slices were excluded in the weighted average. The weighted dry-air mixing ratios are shown for 10 min intervals in Figure 7a,b for the CO_2/H_2O and CH_4/H_2O regions, respectively. For comparison, the measured dry-air mixing ratios from a cavity ringdown point sensor are included. The point sensor samples the outside air within 2 m of the transceivers. As found in our previous studies [4,9], the point sensor measurements overestimate the mixing ratios from addition of local sources of CO_2 and CH_4 that include a utility plant located on the NIST Boulder campus. For dry-air CO_2, the uncertainties range from about 0.3 %

Preprints (www.preprints.org) | NOT PEER-REVIEWED | Posted: 3 October 2023 doi:10.20944/preprints202310.0138.v1

to 1 % over the initial 3+ h measurement period. Interestingly, while the first 120 min showed enhanced backscatter from the clouds and therefore improved residuals, the weighted averages show little in the way of improvement relative to the cloudless regions after the first 120 min. We attribute the lack of improvement to difficulties in splicing the current to the counts for the signal returns that are near the upper dynamic range limit of the PMT. In contrast, the weighted mixing ratios for CH_4 in Figure 7b show substantial improvement in the initial 2.5 h when clouds were present relative to the final 2.5 h when they were absent or too distant. We find the relative uncertainties over the cloud period range from 0.1 % to 0.4 % for CH_4 and increase to 2 % to 3 % in the cloudless period.

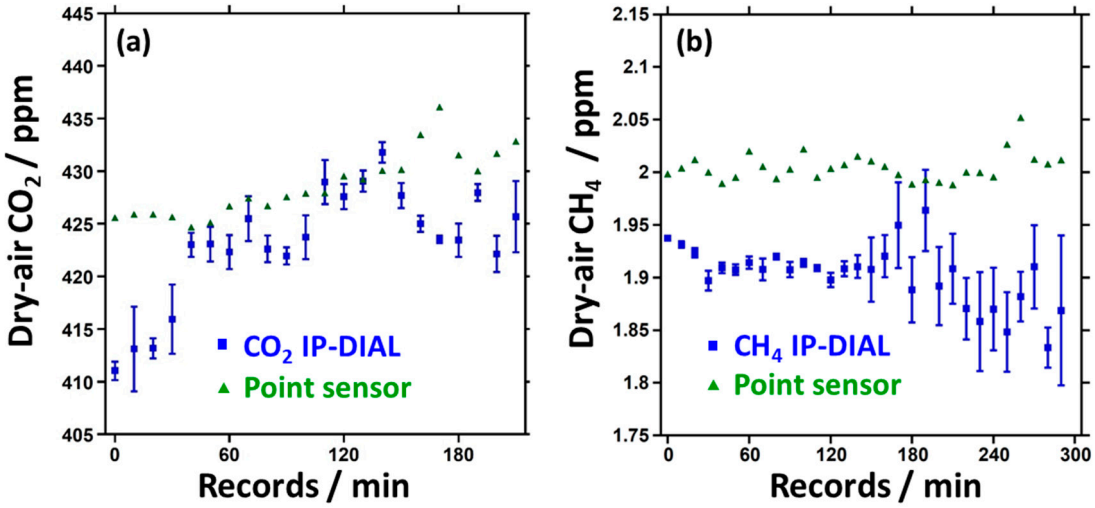

Figure 7. (a) Comparison of the dry-air CO_2 mixing ratios obtained from the slice averaged IPDA data, column averaged DIAL data and the point sensor data over a 3.8 h period on 11/21/2021 and (b) comparison of the dry-air CH_4 mixing ratios obtained from the slice averaged IPDA data, column averaged DIAL data and the point sensor data over a 5 h period on 04/28/2022 (see text for details). Because of the numerous transient emissions likely from a nearby utility plant, the point sensor data in (b) are determined from the baseline values (see Appendix A).

3.3. DIAL Studies of CO_2/H_2O and CH_4/H_2O and comparison with the IP-DIAL results

The range-resolved dry-air concentration maps for CO_2 and H_2O obtained from the DIAL fits using Eq. (1) are shown in Figure 8a,b, respectively and those for CH_4 and H_2O are shown in Figure 8d,e, respectively. Because of technical issues, the results are from the far-field receiver only where full overlap begins near 0.625 km. In both cases, the range resolution is 250 m beginning at 0.75 km and is linearly increased to about 1.5 km at a range of 10 km to help offset the ≈ 1/*R* drop in SNR. The corresponding range-corrected LIDAR maps are shown in the lower panels on an expanded color bar scale which enhances variations in the aerosol backscatter over the first 10 km. Consequently, the cloud aerosol backscatter is off scale as indicated by the absence of color.

Preprints (www.preprints.org) | NOT PEER-REVIEWED | Posted: 3 October 2023 doi:10.20944/preprints202310.0138.v1

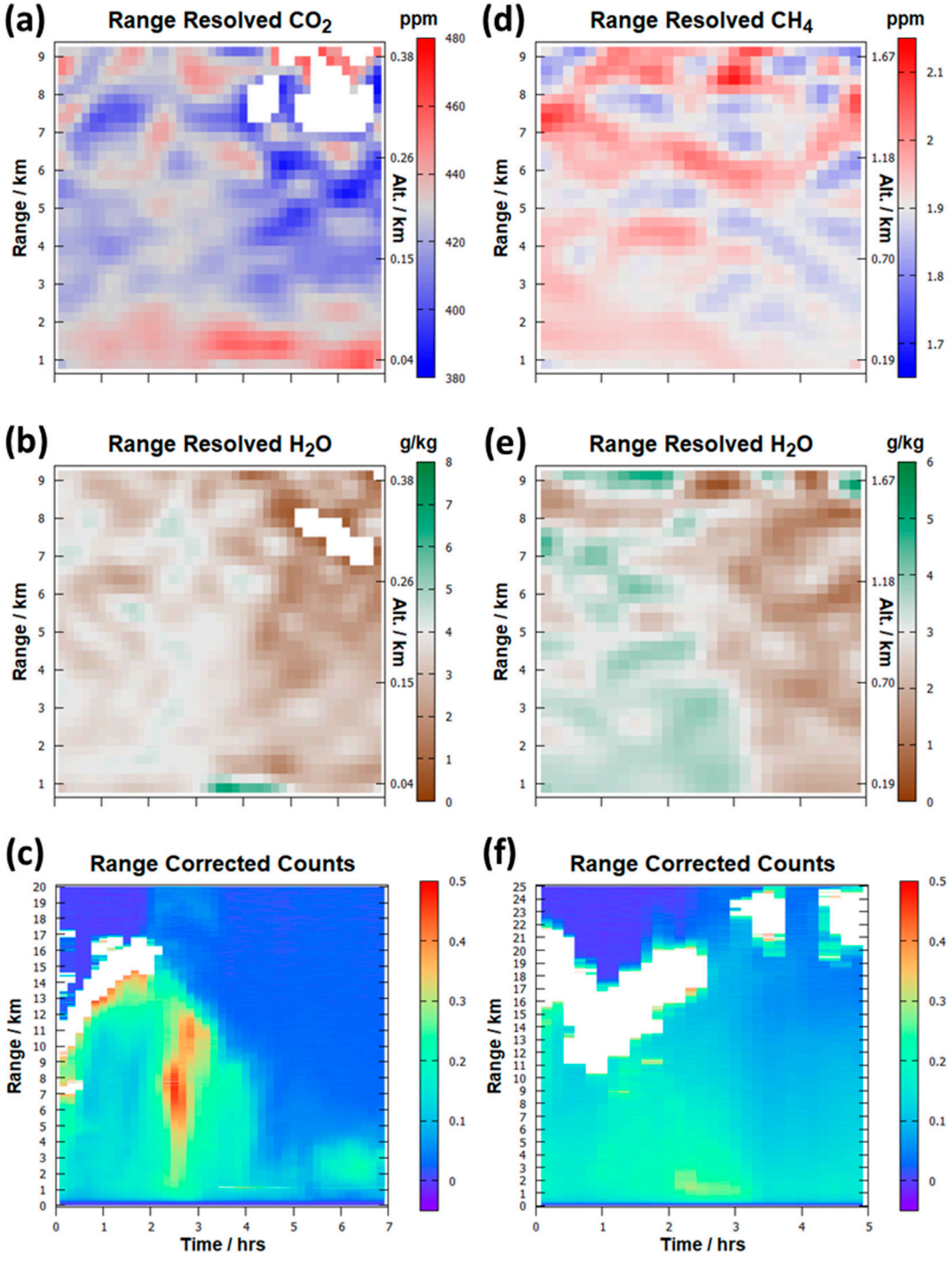

Figure 8. DIAL measurement beginning at 20:32 MST on 11/24/2021 consisting of (a) range-resolved dry-air mixing ratios of CO_2, (b) H_2O near 6241.4 cm^{-1} from 0.75 km to 10 km and (c) range and background corrected offline LIDAR signal returns. DIAL measurements beginning at 21:50 MST on 04/28/2022 consisting of (d) range-resolved dry-air mixing ratios of CH_4, (e) H_2O near 6077.0 cm^{-1} from 0.75 km to 10 km and (f) range and background corrected offline LIDAR signal returns. Missing data are shown as a white background because of very low signal returns.

For the CO_2/H_2O region, the inclination angle is only 2.5° and, at 1.25 km, the beam path is only ≈ 50 m above two emission stacks from a natural gas burning power plant on the University of Colorado campus that was running at full capacity this time of year. As evident in Figure 8) near this

Preprints (www.preprints.org) | NOT PEER-REVIEWED | Posted: 3 October 2023 doi:10.20944/preprints202310.0138.v1

range, particularly in the second half of the measurement period, additional contributions from the plant's plume emission result in a (20-30) ppm increase above the background levels of ≈ 425 ppm. Also apparent in Figure 8c at this range is a sharp and distinct increase (spike) in the LIDAR signals from the plume condensate. A recently reported DIAL study of ours using a fiber amplifier system made use of the emission spike to measure the emission flux from this power plant [36]. We also note in Figure 8c, the abrupt decrease in the LIDAR signal intensity after the first 4 h which reduces the SNR at long range for the latter part of the night. This led to the missing data in regions beyond 7 km as indicated by the absence of color in Figure 8a,b.

A cross check of the DIAL concentration maps can be obtained through comparisons with the IP-DIAL results reported in Section III.2. Given that all data were acquired with the same transceiver system, filter and detector, and that the LPEs are not needed in the DIAL retrievals, differences in the column average mixing ratios from these two independent techniques can provide insight into any systematic errors associated in the data processing and/or assumptions in the models to retrieve concentration. For this, the mixing ratios of the path averaged DIAL (PA-DIAL) data displayed in Figure 8a,b are needed. In contrast to the weighted mean method performed over multiple slices in the cloud region, the range resolved mixing ratios need to be weighted equally and the overall uncertainties must be added in quadrature. For a fixed range bin size of 250 m, the uncertainties would be dominated by the largest uncertainties associated with the weakest returns at long range. As discussed above, the range bin size was linearly increased to largely "equalize" these uncertainties over range.

It is further noted that this comparison is not complete in the sense that the DIAL mixing ratios are missing in the first 0.75 km and for the CH_4/H_2O region, the "gap" between the DIAL data and the IP-DIAL data is too large. Nevertheless, barring any unknown sources and sinks in these regions, the path-averaged values should largely agree with one another.

The comparison of the dry-air mixing ratios of the path averaged DIAL (PA-DIAL) and the IP-DIAL measurements are shown in Figure 9a,b for CO_2 and CH_4, respectively. At most of the 10 min intervals, the PA-DIAL uncertainties for CO_2 and CH_4 range from 1 % to 2 % which are 5- to 10-fold larger than those from the IP-DIAL data. More importantly, IP-DIAL data are well-centered on the PA-DIAL mixing ratios for most of the measurement periods with perhaps a slight bias for lower IP-DIAL values at a few points. Nevertheless, for nearly every interval, the corresponding uncertainties well within those of the PA-DIAL values.

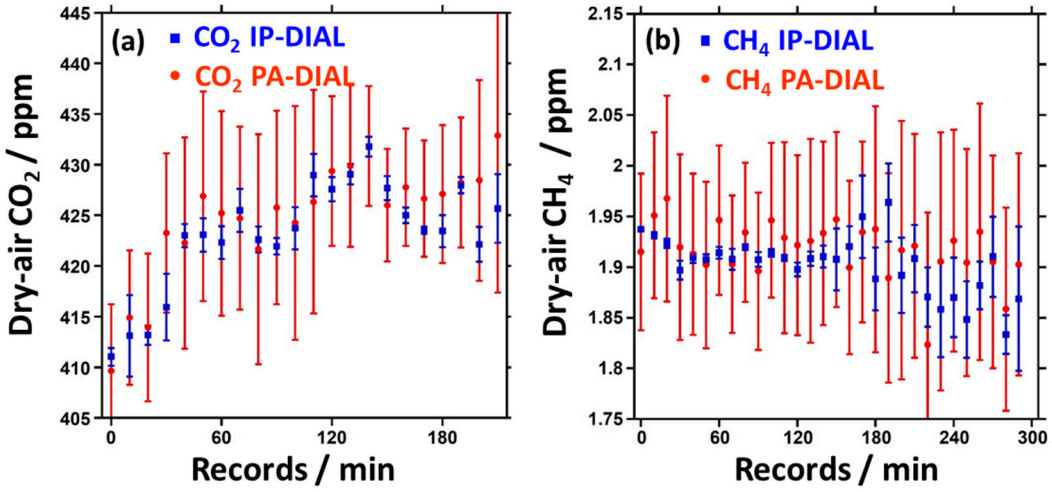

Figure 9. (a) Comparison of the dry-air CO_2 mixing ratios obtained from the slice averaged IP-DIAL data (blue squares) and column averaged DIAL data (C-DIAL) (red dots) over a 3.8 h period on 11/21/2021 and (b) comparison of the dry-air CH_4 concentrations obtained from the slice averaged IP-DIAL data and column averaged DIAL data (red dots) over a 5 h period on 04/28/2022 (see text for details).

Preprints (www.preprints.org) | NOT PEER-REVIEWED | Posted: 3 October 2023 doi:10.20944/preprints202310.0138.v1

4.. Discussion

The measurement uncertainties of the IP-DIAL mixing ratios from cloud aerosol retrievals shown in Figure 7 approach the stringent requirements specified for global satellite measurements to accurately quantify the global changes in GHG mixing ratios and to adequately characterize sources and sinks. However, a few sources of systematic uncertainty (biases) remain in our ground-based spectroscopic studies that prevents us from assigning them as absolute mixing ratio uncertainties.

As mentioned in Section II.3, systematic errors in the form of repeating patterns in the residuals from fits of the CH_4 data to the HITRAN database required us to implement the more refined Hartmann-Tran profile (HTP) [33]. From comparisons of the HTP CH_4 line shape with the HITRAN 2008, 2012, 2016 and 2020, the overall best shape relative to HTP was found for HITRAN 2008 (after scaling the overall peak intensity by 0.98). It is clear from the fit residuals to HITRAN 2008 shown in Figure 10a that the systematic errors are even more pronounced relative to those for HTP in Figure 10b. The HTP integrated line intensity in Ref. [33] was adjusted to that of HITRAN 2020 database which corresponds to a peak intensity reduction of ≈ 0.91 of the HITRAN 2020 profile because of the reduced line broadening in HTP. Since our fits are to peak intensity, this led to > 8 % increase in the best fit mixing ratios of CH_4 relative to HTP. From these comparisons, there is a clear need for an SI standard that is traceable to the World Meteorological Organization (WMO) scale for the absolute intensities of the CH_4 lines. We again note that while the CO_2 profile is also impacted by line mixing and speed dependent effects, the effects on the profile are much smaller relative to CH_4 and are not revealed in the residuals in this study because of the smaller spectral coverage of the online CO_2 measurements.

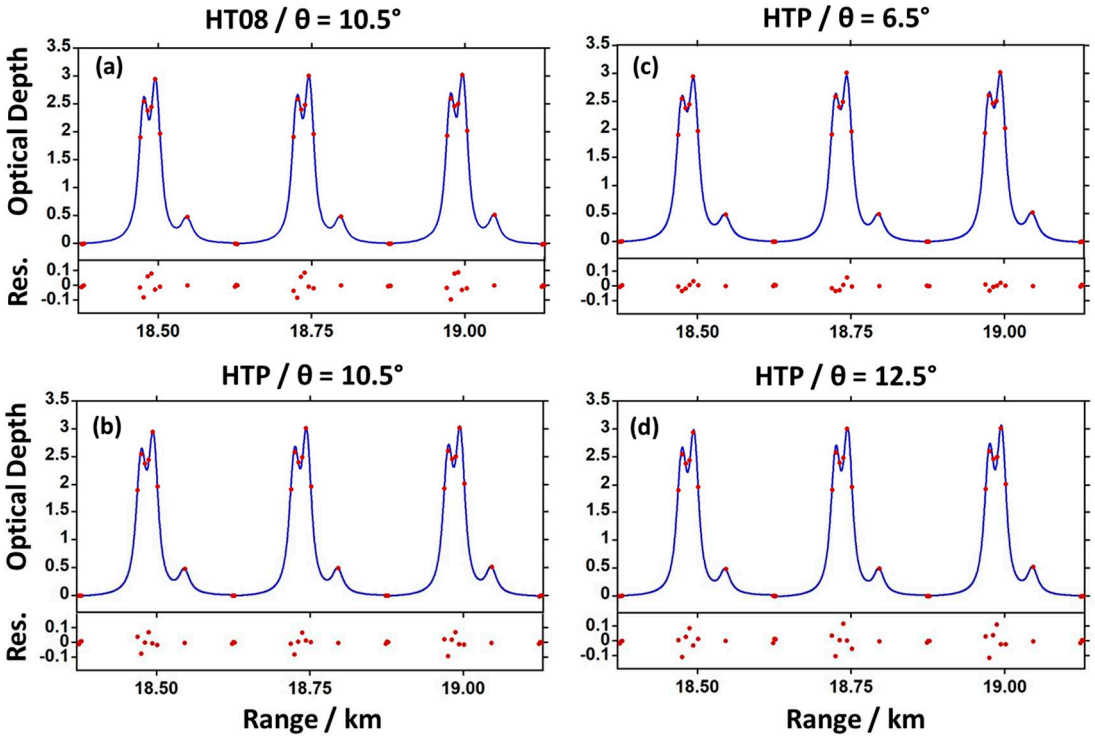

Figure 10. The best-fit CH_4 line shapes using (a) HT08 at the inclination angle, θ = 10.5° (3.4 km in altitude) (b) HTP at θ = 10.5° (3.4 km in altitude), (c) HTP at θ = 6.5° (2.1 km in altitude) and (d) HTP at θ = 12.5° (4.1 km in altitude).

Another unknown that impacts the absolute uncertainties, particularly for the IP-DIAL results of CH_4 at an altitude of ≈ 3.5 km, is in the calculated temperature and pressure (T&P) profile using the U.S. Standard Atmosphere model [29]. While the CO_2 study was performed over a nearly horizontal path where T&P changes along the column are expected to be minimal, some evidence for systematic residuals in the CH_4 line shape residuals remain in Figure 10b. To investigate the impact

Preprints (www.preprints.org) | NOT PEER-REVIEWED | Posted: 3 October 2023 doi:10.20944/preprints202310.0138.v1

the T&P profile, we have refitted this data using two different inclination angles, θ, of 6.5° and 12.5°. The results are shown in Figure 10c,d, respectively. In contrast to the substantial increase in residuals for θ=12.5°, the reduction seen for θ=6.5° is significant. This angle difference of 4° corresponds to an altitude difference of ≈ 1.4 km at a range of 20 km.

Given the strong pressure dependence of the shape of the CH_4 doublet on the residuals, we have performed pressure fits over two series of IP-DIAL line shape profiles. The 10 min intervals chosen are shown in Figure 11c as vertical white lines superimposed on the LIDAR map. The best-fit path-averaged pressures and uncertainties (1σ or Type A, k=1) are shown in Figure 11a,b for the 2nd and 7th intervals, which represent high and low altitude cloud aerosol regions, respectively. The trends expected for the path-averaged T&P profile of the U.S. Standard Atmosphere are superimposed on the plots with yellow and red lines for inclination angles, θ=6.5° and 10.5°, respectively. As found above, the profile for θ=6.5° is in much better agreement with the observed pressure changes. Finally, we also perform pressure fits to profile differences that are separated by 6 km as illustrated by the yellow boxes in Figure 11c. This 6 km separation corresponds to the difference between the cloud ranges in the two columns. We note that as a result of the reduced uncertainties in the cloud regions at 19 km and 13 km in Figure 11a,b, respectively, the relative uncertainties of the pressure fits near the 16 km average range in Figure 11d are significantly reduced. The results shown in Figure 11d are again in much better agreement with the T&P profile at an inclination angle of θ=6.5°.

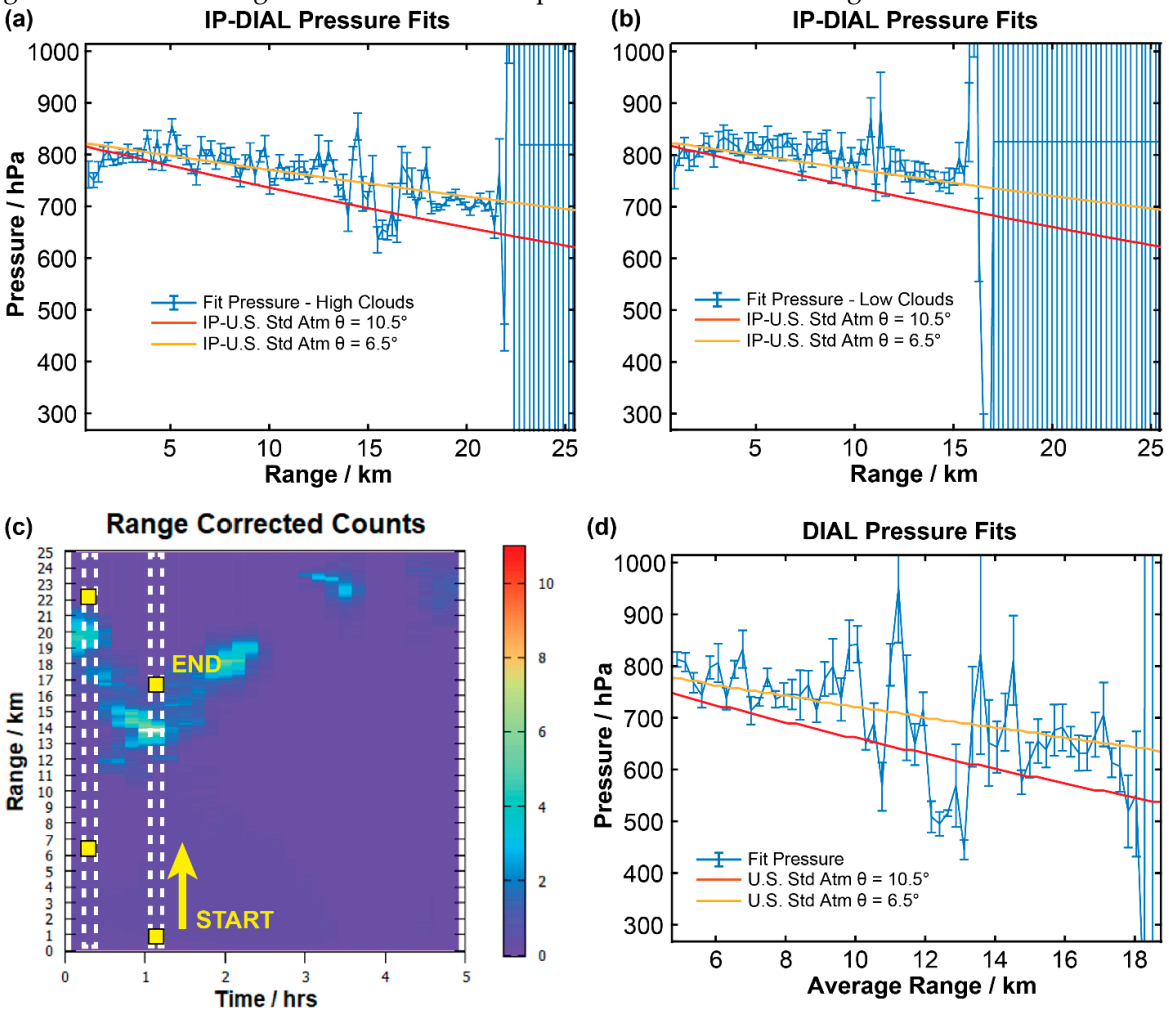

Figure 11. The best-fit path-averaged pressures to a continual IP-DIAL series of line shape profiles for (a) the 2nd 10 min interval and (b) the 7th 10 min interval that sample high and low altitude cloud aerosol regions, respectively. These column intervals are indicated on the LIDAR map in (c) with white dashed vertical lines and the yellow squares indicate the 250 m range bin profiles used as the start and end positions for the pressure fits. The best-fit path-averaged pressures are shown in (d) for

 doi:10.20944/preprints202310.0138.v1

a series of DIAL-like profile differences taken between 250 m range bin profiles spaced by 6 km and shown as a function of the average range defined by the midpoints of these 6 km spacings. In all cases, the error bars represent the 1σ (Type A, k=1) uncertainties obtained directly from the fits. The yellow and red lines in each plot represent the pitch angles (θ) for the path-averaged T&P profiles based on the U.S. Standard Atmosphere.

There may be several possible reasons why the predicted inclination angle from the pressure fits in Figure 11 is about 4° less than the actual inclination angle determined from the platform pitch sensor (which has a confirmed accuracy of ±0.5°). Any effect on the CH_4 line shape that tends to fill in the central dip region will result in fits to higher pressures that will correlate to a lower inclination angle (and lower altitude). One possible mechanism that will fill in the dip region is from additional line broadening by H_2O vapor. The pressure broadening in the HTP model used here is from dry air only. Previous studies [37] have found that CH_4 line widths are, on average, 34 % larger than for dry air under humid conditions (> 5 % relative humidity). However, the relative humidity in this study was relatively low (≈ 1 %) as seen in Figure 8e, and while some additional broadening by H_2O is expected, it is unlikely to account for the observed angle difference of ≈ 4°. A second possibility that will decrease the dip depth is from averaging over the Doppler line shifts associated with changes in wind shear over the integrated path. While a Doppler wind LIDAR system is planned for future measurement campaigns, the only atmospheric wind profile measurements available in this study are from two Denver International Airport (DIA) soundings performed several hours before and after the IP-DIAL study. The wind profile measurements, shown in Appendix B, Figure A1a,b, vary between 11 m/s and 18 m/s at altitudes > 4 km relative to near ground level speeds between 1 m/s and 5 m/s. Over this range, the predicted Doppler frequency shifts for winds parallel to the beam path (i.e., worst case scenario) would be in the range from ±3 MHz to ±10 MHz. Tests on the integrated HTP line shapes over the largest of these shifts indicates the impact on the CH_4 dip depth is small. We also note that the maximum laser frequency shift from the thermal drift the filter cavity over periods longer than these 10 min averaging times is expected to be of this magnitude or less [4]. A final possible reason is the U.S. Standard Atmosphere T&P profile is not a good approximation in this study. Some evidence for this is found from comparisons between the two DIA soundings shown in Appendix B, Figure A3a,b. We note especially the large differences in temperature profiles and an overall pressure shift of ≈ 15 hPa over this 12 h period. Significant differences are also seen relative to the T&P profile of the U.S Standard Atmosphere shown in Figure A3c. Given the impact of a such factors on the online/offline measurements planned for the MERLIN mission [10,11] where such effects will not be evident in the data, current efforts are underway to preform simultaneous 3D wind profile measurements using a Doppler wind LIDAR system and to measure the individual T&P profiles based on the intensity ratio and widths of two nearby water lines.

Finally, we note that while the position of the transceiver platform is controllable, active feedback to track the optimal location for the transmit beam through a cloud region has yet to be implemented. Consequently, the cloud backscatter returns in Figure 3b,d were limited in duration (i.e., 2 h for CO_2 and 2.5 h for CH_4). More importantly, the overall backscatter signal returns were far from optimal; in the CO_2/H_2O region, the offline returns were near the saturation limit of the PMT detection system, which is in sharp contrast to the online returns in the CH_4/H_2O region that were near the noise floor of the detection system. It would clearly be advantageous to work well between these two limiting cases. We expect the SNR ratios will improve significantly once an independent active tracking system under development is completed.

5. Conclusions and Outlook

In this work, we have demonstrated a combined DIAL/IP-DIAL system to measure range-resolved and integrated path mixing ratios of dry-air CO_2 and CH_4 above the city of Boulder, Colorado. The integrated path measurements are performed to cloud targets up to 20 km in range and 3.5 km in altitude. The technique uses 10 frequencies to sample across ≈ 1.5 cm^{-1} spectral regions and to measure the absorption line shapes of CO_2, CH_4 and H_2O as a continuous function of range. A

Preprints (www.preprints.org) | NOT PEER-REVIEWED | Posted: 3 October 2023 doi:10.20944/preprints202310.0138.v1

hybrid photon counting/current detection system enhanced the dynamic range to measure range-resolved backscatter signals from aerosols as well as from distant cloud targets.

The DIAL/IP-DIAL multi-frequency method overcomes two challenging tasks associated with standoff methods. For IP-DIAL, one task is the measurement of the pulse energies with high accuracy at each of the transmitted frequencies. This challenge is overcome through fitting the range resolved DIAL data to extrapolate pulse energies back to the time of emission thereby eliminating the difficulties associated with the uniform unbiased sampling of the transmitted pulses and with the calibration of multiple detectors' responsivities [35]. A second challenge of two-point online/offline DIAL and IP-DIAL systems is with the stringent frequency stabilization of the frequency converter. Because of the multi-frequency sampling and line shape fits performed here, direct determinations of the center frequencies were obtained thereby eliminating systematic errors associated with the OPO seed-signal frequency shift and other thermal drift factors.

Two independent studies were performed in the CO_2/H_2O and CH_4/H_2O regions to simultaneously measure both DIAL and IP-DIAL mixing ratios. Over the cloud aerosol regions, the uncertainties in the IP-DIAL retrievals were found to vary between and 0.2 to 1.0 % for CO_2 and 0.1 % and 1 % for CH_4 while the uncertainties in the range-resolved DIAL measurements varied between 1 % and 2 % in both regions. From a comparison of both techniques, the mixing ratios for the IP-DIAL measurements were found to be well-centered and within the error bars of the DIAL data. Finally, we note that because of the current inability to adjust in real time the transmitter location, the overall signal returns were found to be far from optimal; the backscatter signal intensities were near the detector saturation level in the CO_2/H_2O region while the online returns in the CH_4/H_2O region approached the detector noise floor. Current efforts are directed towards the development of a higher pulse repetition rate LIDAR system operating at 1.6 μm to survey the cloud base and provide active feedback for better positioning of the DIAL/IP-DIAL transceiver system.

Acknowledgments: We gratefully acknowledge funding from the NIST Special Programs Office, James Whetstone, and the Innovation in Measurement Science program at NIST. We also wish to thank Erin Adkins and David Long at NIST for discussions and simulations of the Hartmann-Tran line shape used for CH_4. Special thanks to Martin Stevens, Ryan Cole, and Kimberly Briggman for their detailed comments that have improved the quality of the manuscript.

Appendix A. Picarro Cavity Ringdown and Vaisala Weather Station Measurements

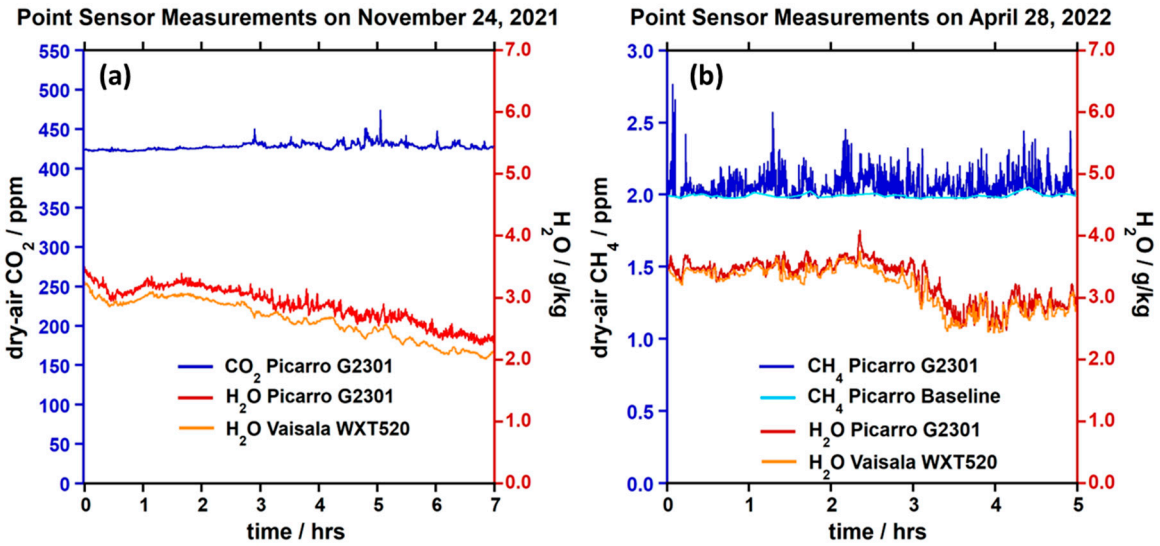

Figure A1. The point sensor measurement of the dry-air mixing ratios of (a) of CO_2 and (b) CH_4 (top traces in blue) and of H_2O (bottom traces: Picarro in red and Vaisala in orange). In (b), the baseline values that underlie the CH_4 data are interpolated to remove contribution from low altitude transients (light blue trace).

Preprints (www.preprints.org) | NOT PEER-REVIEWED | Posted: 3 October 2023 doi:10.20944/preprints202310.0138.v1

The real-time measurements from two point sensors (Picarro cavity ringdown instrument, G2301 and Vaisala weather station, WXT520) that were obtained with a temporal resolution of ≈ 10 sec are shown in Figure A1(a) and A1(b) for CO_2/H_2O and CH_4/H_2O, respectively. In contrast to the relatively smooth trends observed for CO_2/H_2O in Figure A1(a), the large scatter seen for CH_4 in Figure A1(b) is a result of numerous transient emissions near ground level likely from a utility plant located on the Boulder NIST campus in Colorado. These transients lead to significant scatter (> 5 %) when averages were performed over 10 min intervals. Since the local transients are expected to make minor contributions to the IP-DIAL measurements, we have defined the baseline values (light blue trace) in Figure A1(b) to obtain a better representation of the ambient levels for comparisons with the IP-DIAL data. These interpolated baseline values are presented in Figure 7 for comparison with the IP-DIAL results.

Appendix B. Atmospheric Profiles from Airport Soundings

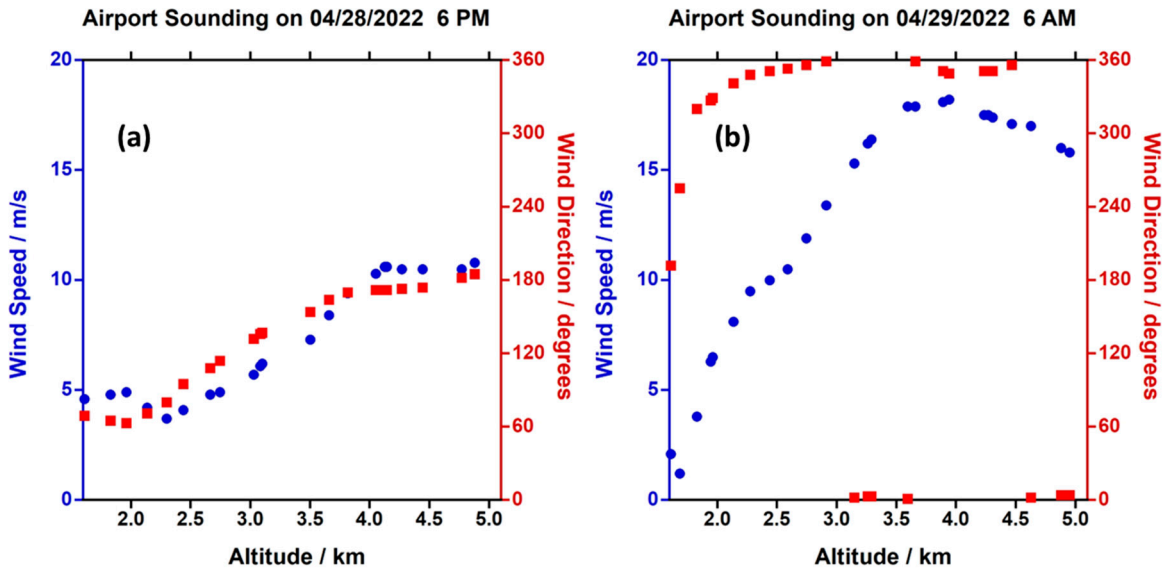

Figure A2. The measured wind speed (blue dots) and direction (red squares) profiles at the Denver International Airport located at 65 km east from the NIST Boulder campus launched on (a) April 28, 2022, at ≈ 6:00 PM and (b) April 29, 2022, at ≈ 6:00 AM. The profiles are shown from the base altitude of 1.6 km in Denver up to an altitude of 5 km, a range that would impact the pressure fits to the CH_4 data in Figure 11.

The Denver International Airport soundings measured on April 28, 2022, at ≈ 6 PM and on April 29, 2022, at ≈ 6 AM are shown in Figure A2a,b respectively. These two soundings bracket the DIAL/IP-DIAL measurements performed on CH_4/H_2O beginning April 28, 2022, at 9:46:58 PM (Epoch: 1651204198).

Preprints (www.preprints.org) | NOT PEER-REVIEWED | Posted: 3 October 2023 doi:10.20944/preprints202310.0138.v1

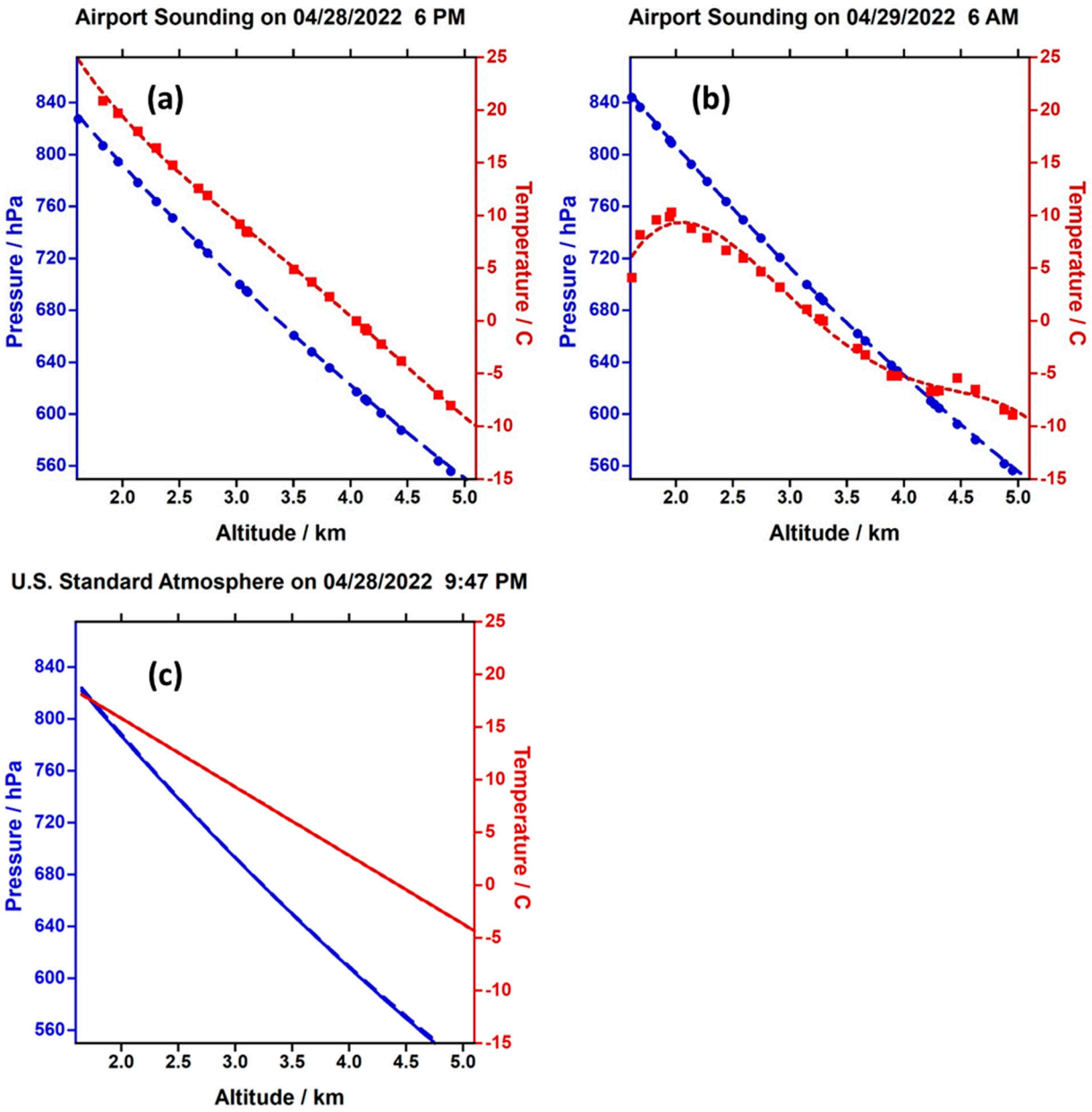

Figure A3. The measured temperature and pressure profiles at the Denver International Airport located at 65 km east from the NIST Boulder campus launched on (a) April 28, 2022, at ≈ 6:00 PM and (b) April 29, 2022, at ≈ 6:00 AM. Curve fits to the data were performed using decaying exponential for pressure and a polynomial of order 4 for temperature. The profiles are shown beginning at the base altitude of 1.6 km in Denver up to an altitude of 5 km, a range that would impact the pressure fits to the CH_4 data in Figure 11. The T&P profiles of the U.S. Standard Atmosphere are shown in (c) for comparison.

The Denver International Airport soundings measured on April 28, 2022, at ≈ 6 PM and on April 29, 2022, at ≈ 6 AM are shown in Figure A3a,b respectively. These two soundings bracket the DIAL/IP-DIAL measurements performed on CH_4/H_2O beginning April 28, 2022, at 9:46:58 PM (Epoch: 1651204198). For this start time, the T&P profile for the U.S. Standard Atmosphere is shown in Figure A3c.

References

1. N. Cezard, S. Le Mehaute, J. Le Gouët, M. Valla, D. Goular, D. Fleury, C. Planchat, and A. Dolfi-bouteyre, "Performance assessment of a coherent DIAL-Doppler fiber lidar at 1645 nm for remote sensing of methane and wind", *Opt. Express*, **28**(15), 22345-22357 (2020).
2. G. J. Koch, J. Y. Beyron, F. Gibert, B. W. Barnes, S. Ismail, M. Petros, P. J. Petzar, J. Yu, E. A. Modlin, K. J. Davis, and U. N. Singh, "Sideline tunable laser transmitter for differential absorption lidar measurements of CO_2: design and application to atmospheric measurements," *Appl. Opt.* **47**, 944–956 (2008).
3. D. Sakaizawa, S. Kawakami, M. Nakajima, T. Tanaka, I. Morino, and O. Uchino, "An airborne amplitude-modulated 1.57 μm differential laser absorption spectrometer: simultaneous measurement of partial column-averaged dry air mixing ratio of CO_2 and target range," *Atmos. Meas. Tech.* **6**, 387–396 (2013).
4. G. A. Wagner and D. F. Plusquellic, "Multi-frequency differential absorption LIDAR system for remote sensing of CO_2 and H_2O near 1.6 μm", *Opt. Express*, **26**, 19420-19434 (2018).
5. A. Amediek, A. Fix, M. Wirth and G. Ehret, "Development of an OPO system at 1.57 μm for integrated path DIAL measurement of atmospheric carbon dioxide", *Appl. Phys. B*, **92**, 295-302 (2008).
6. G. Ehret, C. Kiemle, M. Wirth, A. Amediek, A. Fix, and S. Houweling, "Space-borne remote sensing of CO_2, CH_4, and N_2O by integrated path differential absorption lidar: A sensitivity analysis", *Appl. Phys B*, **90**, 593–608 (2008).
7. J. B. Abshire, A. Ramanathan, H. Riris, J. Mao, G. R. Allan, W. E. Hasselbrack, C. J. Weaver and E. V. Browell, "Airborne measurements of CO_2 column concentration and range using a pulsed direct-detection IPDA Lidar", *Remote Sensing*, **6**, 443-469 (2014).
8. J. Dobler, F. Harrison, E. Browell, B. Lin, D. McGregor, S. Kooi, Y. Choi, S. Ismail, "Atmospheric CO_2 column measurements with an airborne intensity-modulated continuous wave 1.57 um fiber laser lidar", *Appl. Opt.*, **52**, 2874–2892 (2013).
9. G. A. Wagner and D. F. Plusquellic, "Ground-based, integrated path differential absorption LIDAR measurement of CO_2, CH_4, and H_2O near 1.6 μm", *Appl. Opt.*, **55**(23), 6292-6310 (2016).
10. G. Ehret, P. Bousquet, C. Pierangelo, M. Alpers, B. Millet, J. Abshire, *et al.*, "MERLIN: a French-German space lidar mission dedicated to atmospheric methane", *Remote Sensing*, **9**, 1052 (2017).
11. M. Bode, M. Alpers, B. Millet, G. Ehret, and P. Flamant, "MERLIN: an integrated path differential absorption (IPDA) LIDAR for global methane remote sensing," in International Conference on Space Optics (ICSO), Tenerife, Spain, 7–10 October 2014.
12. B. Abshire, H. Riris, G. R. Allan, C. J. Weaver, J. Mao, X. Sun, W. E. Hasselbrack, A. Yu, A. Amediek, Y. Choi, A. Amerdiek, Y. Choi, and E. V Browell. "A lidar approach to measure CO_2 concentrations from space for the ASCENDS Mission", *Proc. SPIE*, 7832 (2010).
13. Y. Durand, J. Caron, P. Bensi, P. Ingmann, J. Bézy, R. Meynart, "A-SCOPE: Concepts for an ESA mission to measure CO_2 from space with a lidar", in Proceedings of the 8th International Symposium on Tropospheric Profiling, Delft, the Netherlands, 19–23 October 2009.
14. B. Yue, S. Yu, M. Li, T. Wei, J. Yuan, Z. Zhang, J. Dong, Y. Jiang, Y. Yang, Z. Gao, and H. Xia, "Local-scale horizontal CO_2 flux estimation incorporating differential absorption lidar and coherent Doppler wind lidar", *Remote Sensing*, **14**, 5150 (2022).
15. A. Amediek, G. Ehret, A. Fix, M. Wirth, C. Büdenbender, M. Quatrevalet, C. Kiemle, C. Gerbig, "CHARM-F a new airborne integrated-path differential-absorption lidar for carbon dioxide and methane observations: Measurement performance and quantification of strong point source emissions", *Appl. Opt.*, **56**, 5182-5197 (2017).
16. H. Riris, K. Numata, S. Li, S. Wu, A. Ramanathan, M. Dawsey, J. Mao, R. Kawa, J. B. Abshire, "Airborne measurements of atmospheric methane column abundance using a pulsed integrated-path differential absorption lidar", *Appl. Opt.*, **51**, 8296-8306 (2012).
17. D. Sakaizawa, S. Kawakami, M. Nakajima, T. Tanaka, L. Morino, and O. Uchino, "An airborne amplitude-modulated 1.57 μm differential laser absorption spectrometer: Simultaneous measurement of partial column-averaged dry air mixing ratio of CO_2 and target range", *Atmos. Meas. Tech.*, **6**, 387-396 (2013).
18. J. Mao, and S. R. Kawa, "Sensitivity study for space-based measurement of atmospheric total column carbon dioxide by reflected sunlight", *Appl. Opt.* **43**, 914–927 (2004).
19. Aben, I.; Hasekamp, O.; Hartmann, W. "Uncertainties in the space-based measurements of CO_2 columns due to scattering in the Earth's atmosphere", *J. Quant. Spectrosc. Radiat. Transf.*, **104**, 450–459 (2007).
20. G. Wagner, A. Behrendt, V. Wulfmeyer, F. Späth, M. Schriller, "High-power Ti:sapphire laser at 820 nm for scanning ground-based water-vapor differential absorption lidar", *Appl. Opt.*, **52**(11), 2454-69 (2013).
21. J. R. Stroud, G. A. Wagner and D. F. Plusquellic, "Validation of a multi-frequency differential absorption LIDAR (DIAL) system from aerosol and cloud retrievals", *CLEO*, paper JW3A.18 (2022).
22. Certain commercial equipment, instruments, or materials are identified in this paper in order to specify the experimental procedure adequately. Such identification is not intended to imply recommendation or endorsement by NIST, nor is it intended to imply that the materials or equipment identified are necessarily the best available for the purpose.

23. R. W. P. Drever, J. L. Hall, F. V. Kowalski, J. Hough, G. M. Ford, A. J. Munley, and H. Ward, "Laser phase and frequency stabilization using an optical resonator," *Appl. Phys. B*, **31**, 97–105 (1983).
24. A. V. Smith and D. J. Armstrong, "Nanosecond optical parametric oscillator with 90° image rotation: design and performance", *J. Opt. Soc. Am. B*, **19**(8), 1801–1814 (2002).
25. D. J. Armstrong and A. V. Smith, "150-mJ 1550-nm KTA OPO with good beam quality and high efficiency", *Proc. SPIE*, **5337**, 71–80 (2004).
26. K. O. Douglass, S. E. Maxwell, D. F. Plusquellic, J. T. Hodges, R. D. van Zee, D. V. Samarov, and J. R. Whetstone, "Construction of a high power OPO laser system for differential absorption LIDAR", *Proc. SPIE*, **8159**, 1–9 (2011).
27. R. K. Newsom, D. D. Turner, B. Mielke, M. Clayton, R. Ferrare, and C. Sivaraman, "Simultaneous analog and photon counting detection for Raman lidar", *Appl. Optics*, **48**, 3903–3914 (2009).
28. I. E. Gordon, L. S. Rothman, R. J. Hargreaves, R. Hashemi, E. V. Karlovets, F.M. Skinner, E. K. Conway, C. Hill, R. V. Kochanov, Y. Tan, P. Wcisło, A .A. Finenko, K. Nelson, P. F. Bernath, M. Birk, V. Boudon, A. Campargue, K. V. Chance, A. Coustenis, B. J. Drouin, J.–M. Flaud, R. R. Gamache, J. T. Hodges, D. Jacquemart, E. J. Mlawer, A. V. Nikitin, V. I. Perevalov, M. Rotger, J. Tennyson, G. C. Toon, H. Tran, V. G. Tyuterev, E. M. Adkins, A. Baker, A. Barbe, E. Canè, A.G. Császár, A. Dudaryonok, O. Egorov, A. J. Fleisher, H. Fleurbaey, A. Foltynowicz, T. Furtenbacher, J. J. Harrison, J.–M. Hartmann, V.–M. Horneman, X. Huang, T. Karman, J. Karns, S. Kassi, I. Kleiner, V. Kofman, F. Kwabia–Tchana, N. N. Lavrentieva, T. J. Lee, D. A. Long, A .A . Lukashevskaya, O. M. Lyulin, V. Yu. Makhnev, W. Matt, S. T. Massie, M. Melosso, S. N. Mikhailenko, D. Mondelain, H. S. P. Müller, O. V. Naumenko, A. Perrin, O. L. Polyansky, E. Raddaoui, P. L. Raston, Z. D. Reed, M. Rey, C. Richard, R. Tóbiás, I. Sadiek, D. W. Schwenke, E. Starikova, K. Sung, F. Tamassia, S. A. Tashkun, J. Vander Auwera, I. A. Vasilenko, A .A. Vigasin, G. L. Villanueva, B. Vispoel, G. Wagner, A. Yachmenev, S. N. Yurchenko, "The HITRAN2020 Molecular spectroscopic database", *J. Quant. Spectrosc. Radiat. Transf.*, **277**, 107949 (2022).
29. NOAA, NASA, and USAF, "U.S. Standard Atmosphere", (1976).
30. R. Gotti, M. Prevedelli, S. Kassi, M. Marangoni, D. Romanini, "Feed-forward coherent link from a comb to a diode laser: application to widely tunable cavity ring-down spectroscopy", *J. Chem. Phys.*, **148**, 054202 (2018).
31. S. Vasilchenko, H. Tran, D. Mondelain, S. Kassi , A. Campargue, "Accurate absorption spectroscopy of water vapor near 1.64 μm in support of the MEthane Remote LIdar missioN (MERLIN)", *J. Quant. Spectrosc. Radiat. Transf.*, **235**, 332-342 (2019).
32. T. Delahaye, S. E. Maxwell, Z. D. Reed, H. Lin, J. T. Hodges, K. Sung, et al. Precise methane absorption measurements in the 1.64 μm spectral region for the MERLIN mission", *J. Geophys. Res. Atmos.*, **121**, 7360-70 (2016).
33. S. Vasilchenko, T. Delahaye, S. Kassi, A. Campargue, R. Armante, H. Tran, D. Mondelain, "Temperature dependence of the absorption of the R(6) manifold of the 2 ν3 band of methane in air in support of the MERLIN mission", *J. Quant. Spectrosc. Radiat. Transf.*, **298**, 108483 (2023).
34. N. H. Ngo, D. Lisak, H. Tran, J-M. Hartmann, "An isolated line-shape model to go beyond the Voigt profile in spectroscopic databases and radiative transfer codes", *J. Quant. Spectrosc. Radiat. Transf.*, **129**, 89-100 (2013).
35. A. Fix, M. Quatrevalet, A. Amediek, M. Wirth, "Energy calibration of integrated path differential absorption lidars", *Appl. Optics*, **57**(26), 7501-7514 (2018).
36. J. R. Stroud, W. J. Dienstfrey and D. F. Plusquellic, "Study on local power plant emissions using multi-frequency differential absorption LIDAR and real time plume tracking", *Remote Sensing*, **15**(17), 4283 (2023).
37. T. Delahaye, X. Landsheere, E. Pangui, F. Huet, J.-M. Hartmann and H. Tran, "Mesaurements of H2O broadening coefficients of infrared methane lines", *J. Quant. Spectrosc. Radiat. Transf.*, **173**, 40-48 (2016).